## scientific reports



### **OPEN**

# Blue photoluminescence from active carboxyl adatoms on nanoporous anodic alumina films

Sam Yeon Cho<sup>1,6</sup>, Kangmo Yeo<sup>1,5,6</sup>, Jin Woo Kim<sup>1</sup>, Jin Ho Kwak<sup>1</sup>, Deok-Yong Cho<sup>1⊠</sup>, Jae Hyuck Jang<sup>2,3⊠</sup>, Sukmin Jeong<sup>1™</sup>, Yong Chan Choi<sup>4™</sup> & Sang Don Bu<sup>1™</sup>

Nanoporous anodic alumina (nPAA) films formed on aluminum in lower aliphatic carboxylic acids exhibit blue self-coloring and characteristic properties such as photoluminescence (PL), electroluminescence, and electron spin resonance. The blue colors are seemingly originated from the adsorbed radicals incorporating into the oxide during the aluminum anodization. However, there is lack of reports revealing the detailed activation mechanism of the adatoms in the complexes. This study investigates the blue PL and its correlation with the atomic and electronic structures of the active aluminum surface using multiple theoretical and experimental methods. The results show that the concentration of carboxylates at the nPAA surface is highly correlated with the blue colorization and manifest that unpaired electrons in carbon (derived from the carboxylates) bridging two aluminum atoms at surface can play as an active source of the blue colorization. Therefore, it is suggested that controlling the adsorption of the carboxylate on the alumina membrane having large surface-to-volume ratio can be an efficient way to generate the blue light for the optoelectronic applications.

Several metals are susceptible to oxidation when exposed to air for extended periods; this process is known as corrosion. This phenomenon results in the formation of an oxide film on the metal surface. The composition and structure of the oxidized film vary depending on the metal and oxidation process. Appropriately controlling the interactions between the metal and surrounding ions within the oxide film can result in the formation of photoluminescent oxide films. For example, nanoporous anodic alumina (nPAA), i.e., a specific type of aluminum oxide, exhibits strong blue photoluminescence (PL) when formed by the anodization of aluminum. This luminescence can be tuned by adjusting the parameters of the controlled anodization process in lower aliphatic carboxylic acids (i.e., carboxylic acids with short alkyl chain)<sup>2–6</sup>. Furthermore, this feature makes nPAA films appealing for diverse applications such as photonic crystals, optical sensors, lasing, and light-emitting diodes<sup>3–8</sup>. Notably, the controllable nanoporous nature of nPAA films enables the tailoring of optical signals in photonic crystals and sensing applications<sup>3–5</sup>. Therefore, unraveling the intricate mechanisms behind PL in these films is critical for optimizing their design and utilizing them in emerging technologies.

Since the initial study of the origin of blue PL in nPAA films by Yamamoto et al.  $^1$ , numerous efforts have focused on understanding and controlling the PL signals in nPAA films, specifically investigating the factors influencing their intensity. The intense blue PL observed in nPAA films formed in oxalic acid is commonly attributed to impurities constituting carboxylates  $^1$ , oxygen vacancies ( $V_O$ ,  $F^+$  and F centers) $^{9-16}$ , and combined effects $^{17-21}$ . While carboxylates (e.g., from oxalic acid) are crucial for the intense blue PL in nPAA films  $^1$ , most research efforts have been devoted to elucidating the role of  $V_O$  and its impact on this type of PL. Consequently, a significant gap remains in our understanding of how carboxylate contribute to the aforementioned phenomenon.

To understand the cooperative role of carboxylates and their concentration control in nPAA films, a wide variety of anodic oxide films have been investigated regarding PL. The study revealed that PL occurred only in nPAA films in specific organic acids containing carboxyl groups (–COOH), unlike those in inorganic acids. The luminescent centers were presumed to be carboxylic ions (or carboxylates), which were incorporated into the films during anodization<sup>1</sup>, rather than singly ionized oxygen vacancies (F<sup>+</sup> centers) in the nPAA films.

¹Department of Physics, Jeonbuk National University, Jeonju 54896, Republic of Korea. ²Electron Microscopy Group for Materials Science, Korea Basic Science Institute, Daejeon 34133, Republic of Korea. ³Graduate School of Analytical Science and Technology, Chungnam National University, Daejeon 34134, Republic of Korea. ⁴Division of Energy Technology, Daegu Gyeongbuk Institute of Science and Technology, Daegu 42988, Republic of Korea. ⁵Present address: Samsung SDI, Yongin 17084, Republic of Korea. ⁶Sam Yeon Cho and Kangmo Yeo contributed equally to this work. email: zax@jbnu.ac.kr; jhjang@kbsi.re.kr; jsm@jbnu.ac.kr; ycchoi@dgist.ac.kr; sbu@jbnu.ac.kr

Furthermore, carboxylates present in various states within the oxide were converted during anodization. This conversion can be attributed to the inhomogeneous distribution of the electric field across the oxide layers. Further investigation into the incorporation mechanism of these carboxylates in anodic oxide films, i.e., the behavior of organic anions during film formation, is required to understand their bonds in anodic oxide films. Here, we consider that the bonds of these carboxylates (COO<sup>-</sup>) in anodic oxide films are nearly the same as that of formate on alumina surface, which is intermediately formed by the reaction of formic acid (oxalic acid) with catalytic alumina, obeying the following reaction scheme:  $COO^- + 2Al = CO^- O + 2Al \Rightarrow C^- O_2 Al_2$  (Fig. S1 of supplementary information)<sup>22</sup>. Similarly, the carboxylate ion is bonded to the film and presumed to exist interstitially in the three-dimensional amorphous network structure.

During the anodization of aluminum, oxalic acid decomposes into carboxylates on the alumina surface<sup>23</sup>. In this case, the bond angle of the  $sp^2$  orbital around carbon (C) in the carboxylate is expected to facilitate the formation of a covalent bond between two oxygen (O) atoms and two aluminum (Al) atoms, rather than forming bonds with a single Al atom. In other words, the breaking of a (resonant)  $\pi$  bond between C and O leaves an empty state on C, which is half-occupied by an electron from O<sup>-</sup>. This unpaired orbital induces a gap state, which is responsible for the blue PL. Therefore, the calculation of the adsorption structure and electronic structure of carboxylate on the alumina surface is essential to reveal the origin of the blue PL.

We studied the bond formation between the carboxyl species and Al in an nPAA film and reported the main chemical species to be the carboxyl free radical with an unpaired electron in C bonded with two Al atoms. The unpaired bond results in a defect level in the energy band gap, likely attributed to the origin of the strong blue PL. The study results show that the room-temperature blue PL emissions of nPAA films can be modulated by anodizing voltages during the fabrication of nPAA films, which is an innovative way of COO<sup>-</sup> concentrations control of nPAA films. More importantly, we suggest that an unpaired electron is present at C, which is different from previous reports supporting that the dangling bond of oxygen is the origin of the PL. The blue PL can be obtained if the unpaired electrons are distributed around a carbon atom. Owing to the presence of unpaired electrons, we present a new adsorption structure for carboxylates.

#### Results and discussion Metal carboxylates in nPAA films

Example text under a subsection. Bulleted lists may be used where appropriate, e.g. To investigate the possible metal carboxylates in nPAA films shown in Fig. 1a (Scanning electron microscopy (SEM) images of nanoporous alumina films synthesized by the anodization of aluminum metal are presented in Figs. S2 and S3), we studied the adsorption and electronic structures (density of states (DOS)) of  $\rm CO_2$  molecules (neutral) and carboxylic ions (one-electron-doped) on  $\rm Al_2O_3$  sapphire surfaces. We adopted a crystalline surface with different orientations (A-, C-, and R-planes) instead of an amorphous  $\rm Al_2O_3$  system because alumina could be locally close to the sapphire surface in the structure. Based on extensive density functional theory calculations, we predicted that the adsorption of the carboxylate could induce a state in the energy gap. Furthermore, the most stable structure on the R-plane represents the bridging bidentate structure, as shown in Fig. 1b and c (Fig. S4 show the comparison results for the bridge structure, metastable structure,  $\rm Al_2O_3$  pristine surface with  $\rm CO_2$  gas, and  $\rm Al_2O_3$  pristine surface). The adsorption of the carboxylate ion induces a state in the energy gap, located at 3.0 eV below the conduction band minimum. The energy gaps from the adsorption of the carboxylate are as small as  $\sim 2.7$  eV above the valence band maximum, originating from structural distortion driven by the carboxylate. The gap state plot reveals that it originates from the carboxylate, mostly localized at the carbon atom, as shown in Fig. 1b (Fig. S5).

Subsequently, the bridging bidentate structure is examined in detail (Fig. S4). The two oxygen atoms forge a bond with surface Al atoms with bond lengths of 1.95 Å, and the carbon atom is outward from the surface. When a carboxylate is adsorbed on the sapphire surface in the bridge structure, a bond between the carboxylate and Al can form instantaneously, with electron transfer from the O atoms to the C atoms. The calculated O–C–O bond angle is 134.6°. The carboxylate is located at the hollow site, bridging the -Al-O- chains along the  $[1\underline{1}01]$  direction. In carboxylates, carbon is usually bonded to a methyl group<sup>24</sup>. In contrast, in the bridging structure, the oxygen atoms favor the surface aluminum atoms (these processes are supposed to be induced by the anodization of aluminum). Thus, the C=O double bond (or resonance) in the carboxylate disappears, with an unpaired electron remaining on the carbon atom (similar to di-bonding<sup>25</sup>).

Next, we estimated the relative formation energy of the bridge structure with respect to the clean surface with  $\rm CO_2$  as a function of the electron chemical potential, i.e., the Fermi level (Fig. S5). The left and right gray regions represent the valence and conduction bands of the bulk sapphire, respectively. Although the surface with  $\rm CO_2$  (no adsorption) is more stable for  $\mu_e < -0.157$  eV (in the electron-poor region), the bridge structure is more stable for  $\mu_e > -0.157$  eV (in the electron-rich region). These results suggest that multiple bridge structures can be formed under electron-rich conditions such as anodization.

The carboxylate molecule that forms the bridge structure has an extra electron in the ionic state before it binds to the alumina; this extra electron is a delocalized electron participating in the resonating  $\pi$ -bonds between the carbon and two oxygen atoms. However, when the carboxylate adsorbs onto alumina and forms a bridge structure, this extra electron is transferred to carbon and becomes an unpaired electron (Figs. S5 and S6). This localized electron forms a half-filled gap. The formation of the bridge structure does not occur when the alumina and carboxylate are electrically neutral because the carbon atom is charged by a surface oxygen atom, forming an O–C bond. However, when additional electrons are supplied through anodization, the negative charge of the carbon atom is stabilized by only two bonds with the oxygen atoms. The unpaired electron state of carbon in the bridge structure is shown in Fig. S6. This allows us to consider that the electrons supplied through anodization play a major role in the adsorption of carboxylates on the alumina surface (formation of the bridge structure).

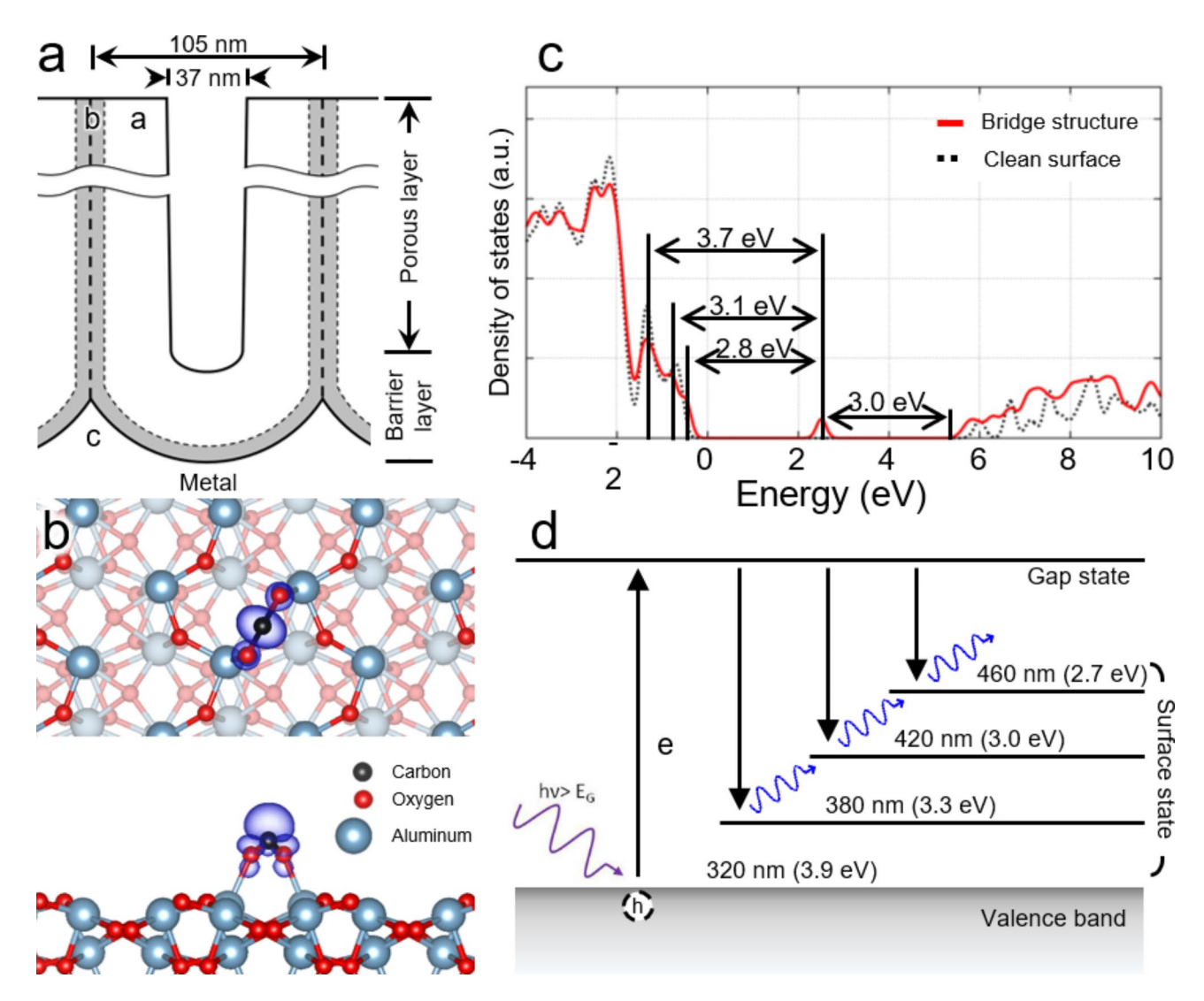


Fig. 1. Theoretical calculations showing the emergence of PL in nanoporous anodic films on aluminum due to possible metal carboxylates, synthesized during the anodization of aluminum metal. (a) Schematic of nanoporous alumina after anodization. (b) Atomic geometry of the bridging bidentate structure with the isosurface of the gap state in (c). The dark and red spheres represent the carbon and oxygen atoms of carboxylate, respectively. The light-colored spheres indicate the substrate atoms, i.e., light-blue and light-red spheres for aluminum and oxygen atoms, respectively. (c) Calculated density of states for the bridging bidentate structure (red curve) with that of the clean surface (dotted curve) as a reference. Energies are referred to the valence band maximum of the clean surface. The bidentate structure induces a gap state around 2.5 eV, which is mainly localized at the C atom. (d) Energy levels of absorption and emission of the structure in (c).

In this bridge structure, the Fermi level straddles the gap state owing to the unpaired electrons in the carbon (Fig. S8). This unusual electronic structure can lead to two types of electronic transition. First, an electron can be excited from the valence band maximum or surface state to the gap state. Second, an electron can be excited from the gap state to the conduction band minimum. The expected energy difference is 2.8–3.7 eV (442–335 nm), which is in the blue light range (Fig. 1d). These results suggest that the carboxylate in the bridge structure can be a source of strong blue PL.

#### Blue luminescence of the nPAA films

To investigate our proposals, we measured the luminescence of the nPAA film anodized at 70 V. Strong blue luminescence was clearly observed with a photograph of the camera and confocal laser scanning microscopy (CLSM) surface images, and stable and adjustable blue PL emission was realized at room temperature in the amorphous transparent nPAA films (Figs. S2 and S3). Blue PL emission in amorphous transparent nPAA films could also be observed directly from the excitation dependence of the PL spectra.

To understand the features of the excited states related to the strong PL emission, we carefully measured the PL spectra at different excitation energies. Figure 2a-d shows the PL emission spectra of the nPAA films as a function of the excitation wavelength (250-380 nm). For the nPAA film excited at 250 nm, two main peaks

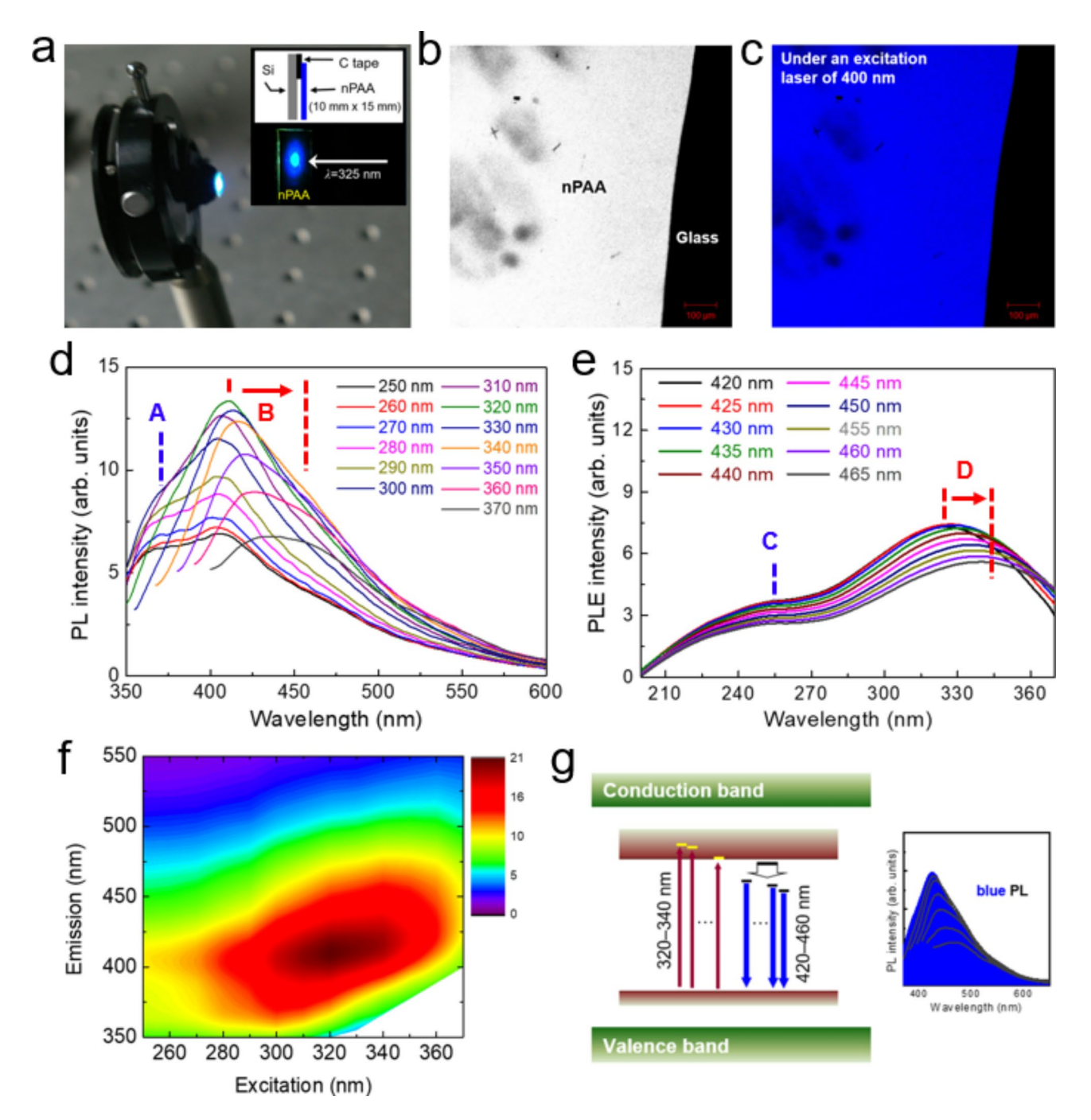


**Fig. 2.** Observation of strong blue PL emission of amorphous nPAA films and their excitation dependence of PL spectra. (**a,b**) A photograph of nPAA film captured under ultraviolet ( $\sim$  325 nm) excitation showing the strong blue color. nPAA films were anodized in lower aliphatic carboxylic acid of oxalic acid ( ${\rm H_2C_2O_4}$ ) (pH: 1.0). (SEM images of nPAA films are shown in Fig. S7). The photograph was captured with a camera (Pentax K100D) using manual mode with a time value of 125 and an aperture value of 8.0. (**c**) Confocal laser CLSM surface images of nPAA film before and after an excitation of 400 nm Ar laser, respectively. CLSM images were obtained using a Zeiss LSM510 META laser scanning microscope. (**d**) PL spectra under various excitation wavelengths and (**e**) PL excitation spectra at various wavelengths of 420–465 nm. (**f**) 2D contour PL intensity map. (**g**) Schematic diagram of the evolution of the PL in the amorphous nPAA films.

were observed: violet emission at 380 nm (marked as A) and blue emission at 420 nm (marked as B). As the excitation wavelength increased from 250 to 320 nm, the intensity of band A decreased, whereas that of band B gradually increased. At an excitation wavelength of 320 nm (green curve), band A almost disappeared, but band B exhibited maximum intensity. Within the range of 330–380 nm, the peak of band B red-shifted from 420 to 460 nm corresponding to a gradual decrease in its intensity.

The corresponding PL excitation spectra monitored at 420–460 nm are shown in Fig. 2e. Two bands corresponding to C and D were observed. Band C remained constant at 250 nm, whereas band D shifted to longer wavelengths ranging from 320 to 340 nm as the emission wavelength increased to 465 nm. From the similar behavior of the PL emission and PL excitation spectra, we conclude that the violet emission (band A) and blue emission (band B) are closely associated with the absorption bands C and D, respectively. Based on these results, the PL emission (band B) corresponding to 420–460 nm is believed to be due to the fact that the gap state is fixed in the bridge structure; however, light of various wavelengths is emitted because the surface states have multiple energy levels. In contrast, the PL emission (band A) corresponding to 380 nm is believed to emit light of only one wavelength, with the same energy as that when the gap state is excited to the conduction band minimum and then returns to the gap state. Based on the results, a 2D contour PL intensity map of the nPAA films was obtained, as shown in Fig. 2f. Next, we proposed possible cases for the energy levels of absorption and emission in the band structure describing the PL evolution in our amorphous nPAA films. Thus, two possible scenarios were considered (Fig. 2g): violet and blue emissions.

#### The local electronic structures adjacent to carboxylate groups within nPAA films

We investigated the local electronic structures adjacent to carboxylate groups within nPAA films using scanning transmission electron microscopy-electron energy loss spectroscopy (STEM-EELS) focused on the C K-edge. Figure 3a shows an annular dark-field (ADF) image of a freestanding nPAA film, revealing its architecture. The image outlines the film's morphology, where dark areas represent pores, and the bright, honeycomb-like networks highlight the structural integrity of the nPAA film. Figure 3b shows the C K-edge intensity profile across these pores, as traced in Fig. 3a. A prominent reduction in intensity at the center to a decreased concentration of carbon within the dense Al,O, regions, particularly in what is designated as the inner layer. This indicates the spatial variance in carbon distribution. The electronic structure of these C K edges is investigated regionally as depicted in Fig. 3c (a), revealing significant differences in the C K-edge obtained from the center compared to points A, B, and C. Notably, at 288–300 eV, there is a significant decrease in the intensity of  $\pi^*$  bonding, suggesting a relative lack of carbon and a lower prevalence of  $\pi^*$  bonds within the honeycomb structures. Such observations align with literature indicating  $\pi^*$  bonding's association with COOH, C=O bonds<sup>26,27</sup>. Through EELS mapping, illustrated in Fig. 3d, we visualized the distribution of  $\pi^*$  bonding in the nPAA structure. As expected, lower distributions were observed within Al<sub>2</sub>O<sub>3</sub> structures, especially at the core, with minimal C-Orelated intensity. Interestingly, carboxylates demonstrated spare concentration around the pores or within the honeycomb-shaped, thick Al<sub>2</sub>O<sub>3</sub> regions identified as the inner layer, predominantly composed of Al<sub>2</sub>O<sub>3</sub>. As revealed through EELS mapping in Fig. 3d, this distribution pattern indicates that carboxylate groups are narrowly present near pores and within honeycomb-structured Al<sub>2</sub>O<sub>3</sub> areas of the nPAA film. Instead, these groups are primarily localized in the intermediary zones between the pore edges and the film's inner layers, a feature prominently highlighted in red on the EELS maps. This mapping emphasizes the carboxylates' spatial preference for intermediary zones, suggesting a distinct interaction between the film's structural configuration and the distribution of functional groups. These findings demonstrate that carboxylates, resulting from the anodization process, have minimal influence on the less etched, dense Al<sub>2</sub>O<sub>3</sub> regions. Thus, it becomes apparent that while carboxylates are marginally concentrated near the pores or within the dense, honeycomb-shaped Al<sub>2</sub>O<sub>3</sub> regions, their primary localization is in the intermediate areas between the pore edges and the inner layers, as emphasized by the red color series (high intensity) in the inset of Fig. 3d. This distribution highlights a subtle understanding of the interplay between the nPAA film's structural characteristics and the electronic properties mediated by carboxylate groups, providing a foundation for further exploration of material modifications through anodization processes.

To prove the effect of the carboxylate (COO-) incorporated in the nPAA films on the blue PL emission, we first examined their concentrations and coordination types, i.e., bonding modes between aluminum and carboxylates, by analyzing Fourier-transform infrared spectroscopy (FT-IR) spectra. In the spectra, four bands at 3500, 2339, 1569, and 1471 cm<sup>-1</sup> were observed (Fig. 4a). The broad band around 3500 cm<sup>-1</sup> corresponded to the stretching vibrations of surface adsorbed hydroxyl groups<sup>28</sup>. (We did flight secondary ion mass spectrometry (TOF-SIMS) data of the PAA samples etched with applied voltages of 20 and 80 V, as shown in Fig. S9. The results show that COOH<sup>-</sup> ions are prevalent in the specimens, which is consistent with the FT-IR data.) The band at 2339 cm<sup>-1</sup> was assigned to the asymmetric stretching vibrations of CO<sub>2</sub> molecules localized in the alumina lattice<sup>29</sup>. The double bands at 1569 and 1471 cm<sup>-1</sup> could be attributed to the asymmetric  $(v_{as})$  and symmetric  $(v_s)$  stretching vibrations of carboxylates (O-C=O or COO<sup>-</sup>), respectively<sup>1,30</sup>. To investigate the bonding mode between Al<sup>3+</sup> and COO<sup>-</sup>, we observed the separation between two vibrations ( $\Delta v = v_{as} - v_{s}$ ). The separation value was between 120 and 122 cm<sup>-1</sup>, suggesting that the carboxylates were coordinated with the aluminum ions in the form of the bridging bidentate (or chelating bidentate)<sup>31</sup>, which was consistent with the atomic geometry (Fig. 1b) provided by the first-principles calculation. We also observed a slight change in the separation value. This slight change indicates that the aluminum carboxylate complex with bridging bidentate coordination is stable in the nPAA films. As shown in Fig. 4b, the concentrations of the double bands of COO- increase as the anodizing voltage increases; but after 70 V, the concentrations decrease. The broad OH and CO<sub>2</sub> molecular bands remain nearly constant, independent of the voltage. The blue PL intensity showed a good relationship with the COO- concentrations, i.e., they changed similarly as the voltage increased. These results show that the roomtemperature blue PL emissions of nPAA films can be modulated by anodizing voltages during the fabrication of nPAA films. Notably, the anodizing voltage is a new way of the COO<sup>-</sup> concentrations control of nPAA films.

#### Conclusion

By combining theoretical and experimental results, this study establishes that carboxylates play a crucial role in the blue PL emission of nPAA films. The unpaired electron on the carbon atom, resulting from the gap state

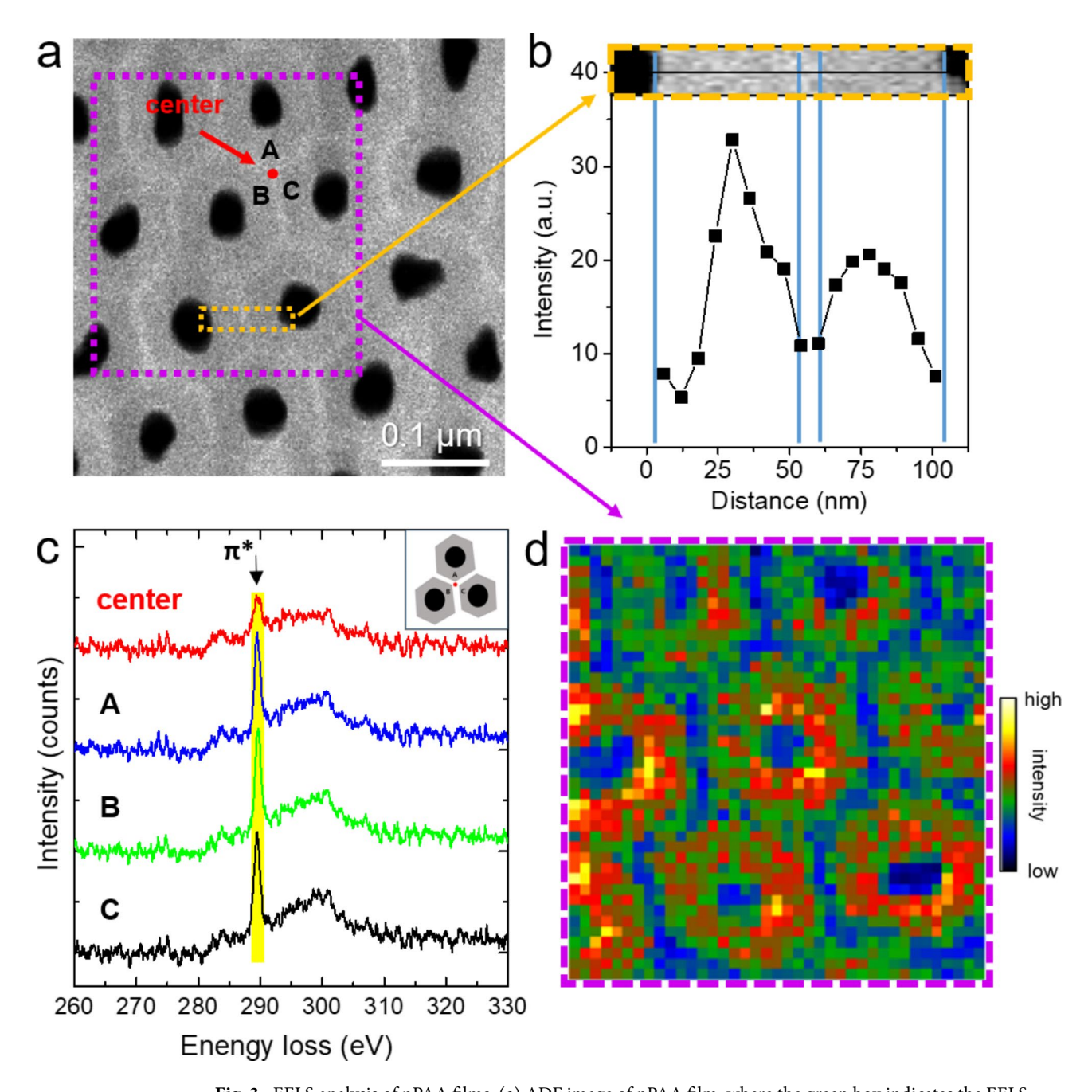


**Fig. 3.** EELS analysis of nPAA films. (a) ADF image of nPAA film, where the green box indicates the EELS mapping area. (b) C K-edge intensity from red line in (a). The C K-edge shows the high counts in the middle regions between pore edges and honeycomb-shaped thick-Al $_2$ O $_3$  regions, as highlighted by red circles at the inset in (b). (c) C K-edges from nPAA region. A, B, C peaks are from the vicinity of pore edges; red C K-edge from center is from the inside of pore wall. (d) Selected energy mapping data (yellow region in the (c)), which reflects carbon chemical bonds with spatial resolution in nPAA region.

induced by carboxylate absorption, is responsible for the characteristic blue light emission. The control of anodizing voltage allows for the modulation of the carboxylate concentration and, consequently, the tuning of the blue PL intensity. These findings provide a comprehensive understanding of the light emission mechanisms in nPAA films and pave the way for the development of novel optoelectric devices.

#### Methods

#### Synthesis and fabrication of nPAA films

nPAA films were fabricated by a two-step anodization and subsequent removal of aluminum. Aluminum sheets with a high level of purity (99.999%) were first degreased in acetone and then electropolished at a constant voltage of 20 V at 5  $^{\circ}$ C for 4 min in a mixture solution of perchloric acid (60% HClO<sub>4</sub>) and ethanol (99.9%)

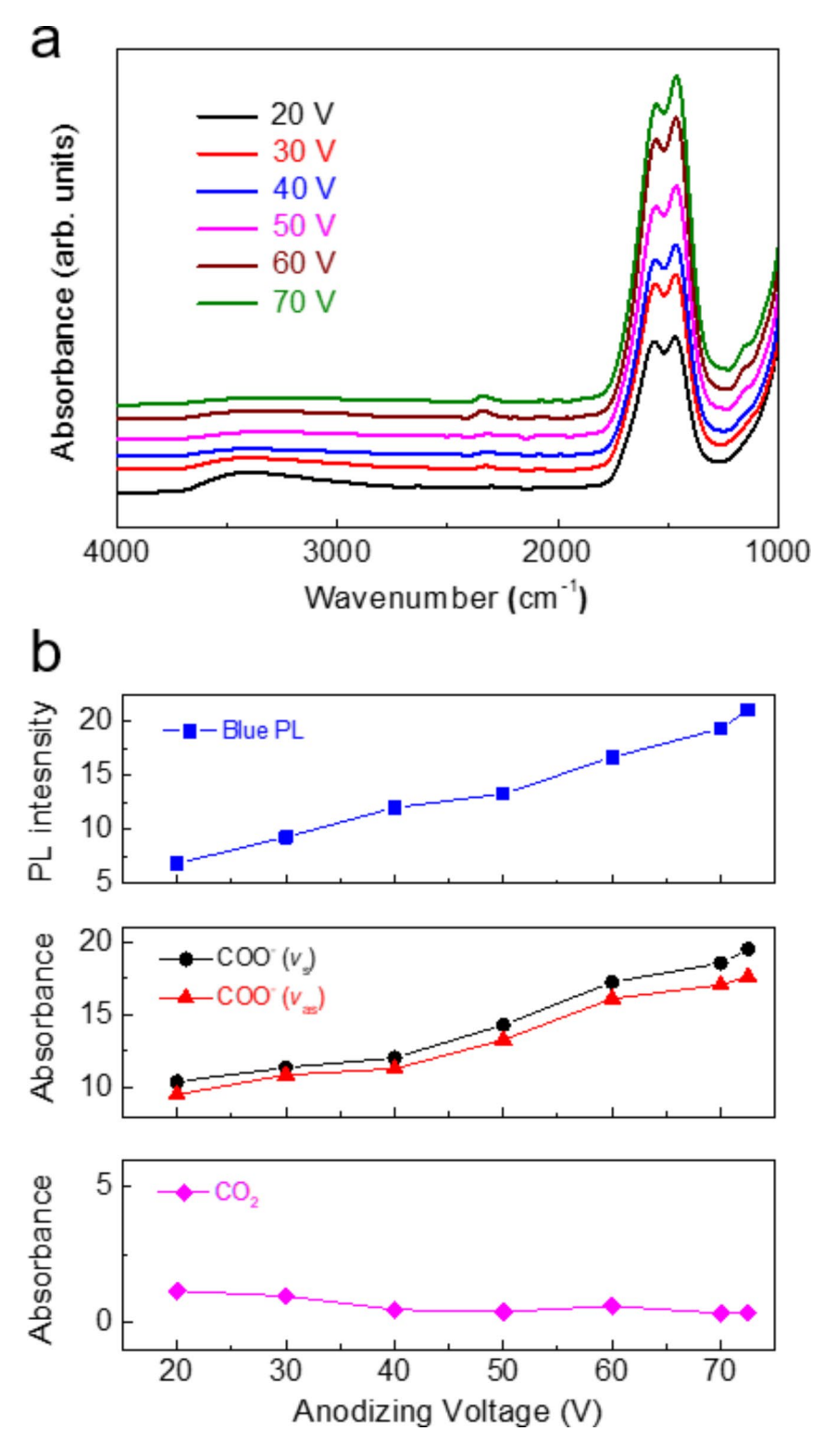


**Fig. 4.** FT-IR spectra as a function of anodizing voltage. (a) FT-IR spectra of nPAA films anodized at voltages of 20–80 V. (b) Variations of COO $^-$  concentrations (or absorbances) with an increasing anodizing voltage, where COO $^-$  ( $\nu_a$ ) and COO $^-$  ( $\nu_s$ ) correspond to the asymmetric and symmetric stretching vibrations of COO $^-$ , respectively. We extracted the COO $^-$  concentrations by obtaining absorbances from the FT-IR peaks in (a) because the concentration was proportional to the absorbance (details can be found in the 2 Methods section).

 ${
m C_2H_5OH}$ ) at a volume ratio of 1:4. Then, the electropolished sheets were anodized at a constant voltage of 20–80 V in 0.3 M oxalic acid at a temperature of 5 °C for 12 h (the first anodization). The irregular nanopores formed during the first anodization were removed by wet chemical etching in an aqueous solution of 6 wt% phosphoric acid ( ${
m H_3PO_4}$ ) and 1.8 wt% chromic acid ( ${
m H_2CrO_4}$ ) at 60 °C for 24 h. The second anodization was performed under the same conditions as the first one, except for the anodization time, to obtain highly ordered nanopores arrays and pore thickness of ~20  ${
m \mu m}$ . After the second anodization, a sample consisting of two distinct layers of nPAA films and aluminum was obtained. To remove the contributions of the interface between the nPAA films and aluminum layers to the PL properties, the films were separated from the sample by dipping them in a saturated  ${
m HgCl_2}$  solution. Finally, these were cleaned with deionized water several times and then heated at 200 °C in vacuum for 1 h to remove the water molecules inside the nPAA nanopores. To check the effects of annealing temperatures on the PL properties, the films were annealed at different temperatures of 300–700 °C for 40 min in a forming gas composed of  ${
m H_2}$  (4%) and  ${
m N_2}$  (96%). For comparison purposes, some of them were annealed at the same temperature ranges in oxygen gas. We found that all films have an amorphous structure as shown in Fig. S10.

#### **CLSM** measurements

CLSM images were obtained using a Zeiss LSM510 META laser scanning microscope under excitation with a 400 nm Ar laser.

#### PL and PL excitation spectra measurements

Room-temperature PL spectra were measured using a He-Cd laser (325 nm wavelength) at a power of 50 mW. The typical results are shown in Fig. S11. Electron paramagnetic resonance (EPR) spectra were recorded using a JES-FA200 *X*-band EPR spectrometer. The PL and PL excitation spectra at different wavelengths were measured using an LS-55 fluorescence spectrometer. The FT-IR spectra were measured with a spectral resolution of 4 cm<sup>-1</sup> over a wavenumber range of 4000–400 cm<sup>-1</sup> (Perkin Elmer, Frontier FT-IR/FIR spectrometer).

#### Calculation methods

All calculations were performed using the Vienna ab initio simulation package (VASP), which incorporated the projector augmented wave (PAW) and generalized gradient approximation (GGA) for the exchange-correlation energy. The surface was simulated using a repeated slab model that included 8 layers of aluminum and 12 layers of oxygen with a vacuum layer of 22.5 Å. To remove the spurious surface states, inversion symmetry was introduced for the supercell. The  $4 \times 4$  periodicity of an ideal surface unit cell and a  $4 \times 4$  k-point mesh in the surface Brillouin zone were used. A plane-wave basis was used with a cutoff energy of 30 Ry.

#### FT-IR measurements

We extracted the concentrations of Al metal carboxylates by obtaining the absorbance from the FT-IR peak at a specific wavenumber because the absorbance was proportional to the concentration<sup>32</sup>. The absorbance A can be calculated using the equation  $A = \log{(1/T)}$ , where T is the transmittance. The coordination type could be identified by the magnitude of the separation between the asymmetric and symmetric stretching vibrations of  $COO^{-33}$ .

#### **TEM and EELS measurements**

The local electronic structures near the carboxylates were examined using STEM-EELS at the C *K* edge (Libra 200 HT Mc Cs). The microstructures of the nPAA films were examined using high-resolution TEM (HRTEM, JEOL, JEM-2100 F) equipped with a field-emission gun.

#### Data availability

All data generated or analysed during this study are included in this published article and its supplementary information files. The datasets used and/or analysed during the current study available from the corresponding author on reasonable request.

#### Received: 12 November 2024; Accepted: 17 January 2025

#### Published online: 22 January 2025

#### References

- Yamamoto, Y., Baba, N. & Tajima, S. Coloured materials and photoluminescence centres in anodic film on aluminium. *Nature* 289, 572–574. https://doi.org/10.1038/289572a0 (1981).
- Santos, A. et al. Structural tuning of photoluminescence in nanoporous anodic alumina by hard anodization in oxalic and malonic acids. Nanoscale Res. Lett. 7, 228. https://doi.org/10.1186/1556-276X-7-228 (2012).
- Santos, A., Kumeria, T. & Losic, D. Optically optimized photoluminescent and interferometric biosensors based on nanoporous anodic alumina: A comparison. Anal. Chem. 85, 7904–7911. https://doi.org/10.1021/ac401609c (2013).
- 4. Lim, S. Y. et al. Engineering nanoporous anodic alumina bilayered interferometers for liquid and gas sensing. ACS Appl. Nano Mater. 6, 20954–20969. https://doi.org/10.1021/acsanm.3c03978 (2023).
- Law, C. S., Santos, A., Nemati, M. & Losic, D. Structural engineering of nanoporous anodic alumina photonic crystals by sawtooth-like pulse anodization. ACS Appl. Mater. Interfaces 8, 13542–13554. https://doi.org/10.1021/acsami.6b03900 (2016).
- Acosta, L. K., Law, C. S., Santos, A., Ferré-Borrull, J. & Marsal, L. F. Tuning intrinsic photoluminescence from light-emitting multispectral nanoporous anodic alumina photonic crystals. *APL Photonics* 7, 026108. https://doi.org/10.1063/5.0078505 (2022).
   Lee, H., Hong, A., Kwak, J. & Lee, S. Synthesis of UV/blue light-emitting aluminum hydroxide with oxygen vacancy and their
- application to electrically driven light-emitting diodes. RSC Adv. 12, 4322–4328. https://doi.org/10.1039/D1RA07942E (2022).
- 8. Bai, X. et al. Efficient and tuneable photoluminescent boehmite hybrid nanoplates lacking metal activator centres for single-phase white LEDs. *Nat. Commun.* 5, 5702. https://doi.org/10.1038/ncomms6702 (2014).

- 9. Du, Y. et al. Preparation and photoluminescence of alumina membranes with ordered pore arrays. *Appl. Phys. Lett.* **74**, 2951–2953. https://doi.org/10.1063/1.123976 (1999).
- Li, Y., Li, G., Meng, G., Zhang, L. & Phillipp, F. Photoluminescence and optical absorption caused by the F+ centres in anodic alumina membranes. J. Phys. Condens. Matter 13, 2691. https://doi.org/10.1088/0953-8984/13/11/323 (2001).
- 11. Huang, G., Wu, X., Mei, Y., Shao, X. & Siu, G. Strong blue emission from anodic alumina membranes with ordered nanopore array. J. Appl. Phys. 93, 582–585. https://doi.org/10.1063/1.1529075 (2003).
- 12. Green, S. et al. Optical properties of nanoporous Al<sub>2</sub>O<sub>3</sub> obtained by aluminium anodization. *Phys. Status Solidi C* **4**, 618–621. https://doi.org/10.1002/pssc.200673298 (2007).
- 13. Khan, G. G., Singh, A. K. & Mandal, K. Structure dependent photoluminescence of nanoporous amorphous anodic aluminium oxide membranes: Role of F<sup>+</sup> center defects. *J. Lumin.* 134, 772–777. https://doi.org/10.1016/j.jlumin.2012.06.050 (2013).
- 14. Choudhari, K. S., Kulkarni, S. D., Santhosh, C. & George, S. D. Photoluminescence enhancement and morphological properties of nanoporous anodic alumina prepared in oxalic acid with varying time and temperature. *Microporous Mesoporous Mater.* 271, 138–145. https://doi.org/10.1016/j.micromeso.2018.06.004 (2018).
- 15. Cantelli, L. et al. Unveiling the origin of photoluminescence in nanoporous anodic alumina (NAA) obtained by constant current regime. *J. Lumin.* 207, 63–69. https://doi.org/10.1016/j.jlumin.2018.10.015 (2019).
- Reddy, P. R., Ajith, K. M. & Udayashankar, N. K. Effect of electrolyte concentration on morphological and photoluminescence properties of free standing porous anodic alumina membranes formed in oxalic acid. *Mater. Sci. Semicond. Process.* 106, 104755. https://doi.org/10.1016/j.mssp.2019.104755 (2020).
- 17. Xu, W., Zheng, M., Wu, S. & Shen, W. Effects of high-temperature annealing on structural and optical properties of highly ordered porous alumina membranes. *Appl. Phys. Lett.* **85**, 4364–4366. https://doi.org/10.1063/1.1815072 (2004).
- 18. Xu, W., Chen, H., Zheng, M., Ding, G. & Shen, W. Optical transmission spectra of ordered porous alumina membranes with different thicknesses and porosities. *Opt. Mater.* 28, 1160–1165. https://doi.org/10.1016/j.optmat.2005.07.003 (2006).
- Li, Z. & Huang, K. Blue luminescence in porous anodic alumina films. J. Phys. Condens. Matter 19, 216203. https://doi.org/10.108 8/0953-8984/19/21/216203 (2007).
- Li, Z. & Huang, K. Optical properties of alumina membranes prepared by anodic oxidation process. J. Lumin. 127, 435–440. https://doi.org/10.1016/j.jlumin.2007.02.001 (2007).
- 21. Li, Z. & Huang, K. The effect of high-temperature annealing on optical properties of porous anodic alumina formed in oxalic acid. *Luminescence* 22, 355–361. https://doi.org/10.1002/bio.971 (2007).
- 22. Hirota, K., Fueki, K., Shindo, K. & Nakai, Y. Studies on the state of formic acid adsorbed on silica and alumina by a combined method of nuclear magnetic resonance and infrared absorption. *Bull. Chem. Soc. Jpn.* 32, 1261–1263. https://doi.org/10.1246/bcsj.32.1261 (1959).
- Scialdone, O., Galia, A., Guarisco, C., Randazzo, S. & Filardo, G. Electrochemical incineration of oxalic acid at boron doped diamond anodes: Role of operative parameters. *Electrochim. Acta* 53, 2095–2108. https://doi.org/10.1016/j.electacta.2007.09.007 (2008)
- 24. March, J. Advanced Organic Chemistry: Reactions, Mechanisms, and Structure 4th edn. (Wiley, 1992).
- 25. Cao, Y., Wei, X. M., Chin, W. S., Lai, Y. H. & Xu, G. Q. Formation of di-σ bond in benzene chemisorption on Si(111)-7×7. *J. Phys. Chem. B* 103, 5698–5702. https://doi.org/10.1021/jp990479l (1999).
- Rabchinskii, M. K. et al. Graphene oxide conversion into controllably carboxylated graphene layers via photoreduction process in the inert atmosphere. Fuller. Nanotub. Carbon Nanostruct. 28, 221–225. https://doi.org/10.1080/1536383X.2019.1686625 (2020).
- 27. Ye, Y. et al. X-ray absorption spectroscopy characterization of a Li/S cell. Nanomaterials 6, 14. https://doi.org/10.3390/nano6010014 (2016)
- 28. Nakamoto, K. Infrared and Raman Spectra of Inorganic and Coordination Compound (Academic Press, 1986).
- 29. Mardilovich, P. P., Govyadinov, A. N., Mukhurov, N. I., Rzhevskii, A. M. & Paterson, R. New and modified anodic alumina membranes Part I. Thermotreatment of anodic alumina membranes. *J. Membr. Sci.* **98**, 131–142. https://doi.org/10.1016/0376-738 8(94)00184-Z (1995).
- 30. Yamamoto, Y. & Baba, N. Nature of the carboxylate species incorporated in anodic alumina films formed in oxalic acid solution. *Thin Solid Films* **101**, 329–338. https://doi.org/10.1016/0040-6090(83)90099-8 (1983).
- Dobson, K. D. & McQuillan, A. J. In situ infrared spectroscopic analysis of the adsorption of aliphatic carboxylic acids to TiO<sub>2</sub>, ZrO<sub>2</sub>, Al<sub>2</sub>O<sub>3</sub>, and Ta<sub>2</sub>O<sub>5</sub> from aqueous solutions. Spectrochim. Acta A 55, 1395–1405. https://doi.org/10.1016/S1386-1425(98)00303-5 (1999).
- 32. Smith, B. C. Infrared Spectral Interpretation: A Systematic Approach (CRC Press, 1998).
- 33. Deacon, G. B. & Phillips, R. J. Relationships between the carbon-oxygen stretching frequencies of carboxylato complexes and the type of carboxylate coordination. *Coord. Chem. Rev.* 33, 227–250. https://doi.org/10.1016/S0010-8545(00)80455-5 (1980).

#### **Acknowledgements**

This work was supported by the National Research Foundation of Korea (NRF) grant funded by the Korea government (MSIT) (No. NRF-2021R1A2C2011350).

#### **Author contributions**

S.Y.C.: Investigation, Conducted the experiment, Formal analysis, K.Y.: Investigation, Formal analysis, J.W.K.: Conducted the experiment, D.-Y.C.: Formal analysis, Data curation, Conceptualization, J.H.J.: Formal analysis, Data curation, Conceptualization, Y.C.C.: Investigation, Formal analysis, Writing original draft. S.D.B.: Investigation, Supervision, Conceptualization. All authors reviewed the manuscript.

#### **Declarations**

#### Competing interests

The authors declare no competing interests.

#### Additional information

**Supplementary Information** The online version contains supplementary material available at https://doi.org/1 0.1038/s41598-025-87342-8.

Correspondence and requests for materials should be addressed to D.-Y.C., J.H.J., S.J., Y.C.C. or S.D.B.

**Reprints and permissions information** is available at www.nature.com/reprints.

**Publisher's note** Springer Nature remains neutral with regard to jurisdictional claims in published maps and institutional affiliations.

**Open Access** This article is licensed under a Creative Commons Attribution-NonCommercial-NoDerivatives 4.0 International License, which permits any non-commercial use, sharing, distribution and reproduction in any medium or format, as long as you give appropriate credit to the original author(s) and the source, provide a link to the Creative Commons licence, and indicate if you modified the licensed material. You do not have permission under this licence to share adapted material derived from this article or parts of it. The images or other third party material in this article are included in the article's Creative Commons licence, unless indicated otherwise in a credit line to the material. If material is not included in the article's Creative Commons licence and your intended use is not permitted by statutory regulation or exceeds the permitted use, you will need to obtain permission directly from the copyright holder. To view a copy of this licence, visit <a href="https://creativecommons.org/licenses/by-nc-nd/4.0/">https://creativecommons.org/licenses/by-nc-nd/4.0/</a>.

© The Author(s) 2025